Differential and integral cross sections in OH(X) + Xe collisions

Gautam Sarma, Ashim Kumar Saha, J. J. ter Meulen, David H. Parker, and Sarantos Marinakis

Citation: The Journal of Chemical Physics **142**, 034309 (2015); doi: 10.1063/1.4906070
View online: http://dx.doi.org/10.1063/1.4906070
View Table of Contents: http://scitation.aip.org/content/aip/journal/jcp/142/3?ver=pdfcov
Published by the AIP Publishing

Differential and integral cross sections in OH(X) + Xe collisions

Gautam Sarma,[1] Ashim Kumar Saha,[1] J. J. ter Meulen,[1] David H. Parker,[1,a)] and Sarantos Marinakis[2,b)]

[1]*Institute for Molecules and Materials, Radboud University Nijmegen, Heijendaalseweg 135, 6525 ED Nijmegen, The Netherlands*

[2]*School of Biological and Chemical Sciences, Queen Mary University of London, Joseph Priestley Building, Mile End Road, London E1 4NS, United Kingdom*

(Received 2 November 2014; accepted 30 December 2014; published online 21 January 2015)

Differential cross sections (DCSs) for inelastic collisions of OH(X) with Xe have been measured at a collision energy of 483 cm^{-1}. The hydroxyl (OH) radicals were initially prepared in the $X^2\Pi_{3/2}$ ($v = 0$, $j = 1.5$, f) level using the hexapole electric field selection method. Products were detected state-selectively by [2 + 1] resonance-enhanced multiphoton ionization of OH, combined with velocity-map imaging. Integral cross sections in OH(X) + Xe at a collision energy of 490 cm^{-1} were also measured by laser-induced fluorescence. The results are compared with exact close-coupling quantum mechanical scattering calculations on the only available *ab initio* potential energy surface (PES). The agreement between experimental and theoretical results is generally very satisfactory. This highlights the ability of such measurements to test the available PES for such a benchmark open-shell system. The agreement between experiment and theory for DCSs is less satisfactory at low scattering angles, and possible reasons for this disagreement are discussed. Finally, theoretical calculations of OH(X) + He DCSs have been obtained at various collision energies and are compared with those of OH(X) + Xe. The role of the reduced mass in the DCSs and partial cross sections is also examined. © *2015 AIP Publishing LLC.* [http://dx.doi.org/10.1063/1.4906070]

I. INTRODUCTION

Collisions of radicals such as hydroxyl (OH) play a crucial role in many chemical systems, including interstellar chemistry,[1] combustion,[2] and atmospheric reactions.[3] An important component in the mechanism of such processes involving hydroxyl is rotational energy transfer (RET) by collisions with other molecules. In addition to RET processes, collisions that transfer populations between spin-orbit and Λ-doublet levels are also possible because of the complex energy-level structure of OH(X).[4] This additional complexity has attracted accurate quantum-state resolved theoretical scattering studies on collisions of OH with rare-gas atoms.[5–7] Previous experimental studies on these OH(X) collisions have used mainly laser-induced fluorescence (LIF), which is extremely sensitive, but its successful application for providing the correlation between initial and final velocity vectors has been limited for various technical reasons.[8]

As shown in a recent review by Costen *et al.*,[9] additional information for these systems can be obtained by measuring vector properties, such as the differential cross section (DCS), which is proportional to the probability of scattering at a given angle between the initial and final relative velocity vectors. A method that can provide the DCS for collisions of OH(X) has quite recently been presented by Sarma *et al.*[8] This method couples [2+1] resonance-enhanced multiphoton ionization (REMPI) of OH(X) with velocity-map imaging (VMI) and has been applied successfully to the study of OH(X) + Ar/He collisions. This paper extends the study described in our previous paper to the much less studied collisions of OH(X) with Xe atoms. The only available *ab initio* potential energy surface (PES) for this system has been constructed by Groenenboom[5] using the restricted open-shell coupled cluster [RCCSD(T)] method. This PES was able to reproduce the relative inelastic integral cross sections (ICSs) measured by Stark-decelerated molecular-beam experiments in the Meijer group (Berlin) at collision energies between 50 and 400 cm^{-1}.[5,7] That PES was also used by McKendrick and co-workers to obtain population transfer rate coefficients for collisions of OH(X) + Xe at room temperature (298 K).[10]

In this paper, measurements of the differential and integral cross sections in collisions of OH(X) with Xe atoms at a collision energy of 483 cm^{-1} and 490 cm^{-1}, respectively, are presented. In Sec. II, details of the experimental and data analysis methods employed are described. The experimental results are compared with quantum scattering calculations performed at the same collisional energies. The calculations provided state-to-state differential and integral cross sections for all possible post-collisional OH(X) rotational levels. The theoretical aspects of the present work are described in Sec. II B, and the results on ICS and DCS are presented in Sec. III. In Sec. IV, we compare our experimental and theoretical data

a)Electronic mail: parker@science.ru.nl.

b)Author to whom correspondence should be addressed. Electronic mail: s.marinakis@qmul.ac.uk. This research was started while S. Marinakis was at Department of Chemistry, The Physical and Theoretical Chemistry Laboratory, University of Oxford, South Parks Road, Oxford OX1 3QZ, United Kingdom.

with previous work on similar systems and examine the role of reduced mass in the DCS. Section V summarizes our main conclusions.

II. METHODS

A. Experimental

1. Production of state-selected OH(X) radicals

OH(X) radicals are produced by an electrical discharge in the expanding mixture of Ar and H_2O at the exit of a Jordan pulsed valve nozzle (see Fig. 1). A pulsed voltage of 1 kV is applied to a pair of stainless steel plates attached to the valve nozzle. This potential difference is applied for duration of 60 μs, which is shorter than the 100 μs opening duration of Jordan valve. Both the pulsed discharge and molecular valve are working at 10 Hz repetition rate. A filament is placed adjacent to the discharge assembly and a current of around 1 A is passed through it. This glowing filament emits electrons that help to initiate and stabilize the discharge. The discharge produced OH beam is passed through a skimmer with an opening of 3 mm diameter placed 2.5 mm away from the discharge assembly. The skimmer is supplied with a voltage of −300 V to deflect the ions formed in the discharge.

As shown in Fig. 2, the ground electronic state of OH radicals has two spin-orbit states; the $^2\Pi_{1/2}$ with $\Omega = 1/2$ and the $^2\Pi_{3/2}$ with $\Omega = 3/2$, with the latter being lower in energy. The rotational manifolds which arise from the lower and higher spin-orbit states are termed F_1 and F_2, respectively. Each rotational level is split into two Λ-doublet components, which are nearly degenerate with opposite parities, $+(-1)^{j-1/2}$ or $-(-1)^{j-1/2}$, denoted e or f, respectively. The notation j e/f F_1/F_2 is used hereafter to describe the rotational levels of OH(X) radicals. After passing the skimmer, the OH molecules are 99.5% in the lowest Λ-doublet, i.e., in the 1.5eF_1 and 1.5fF_1 levels.

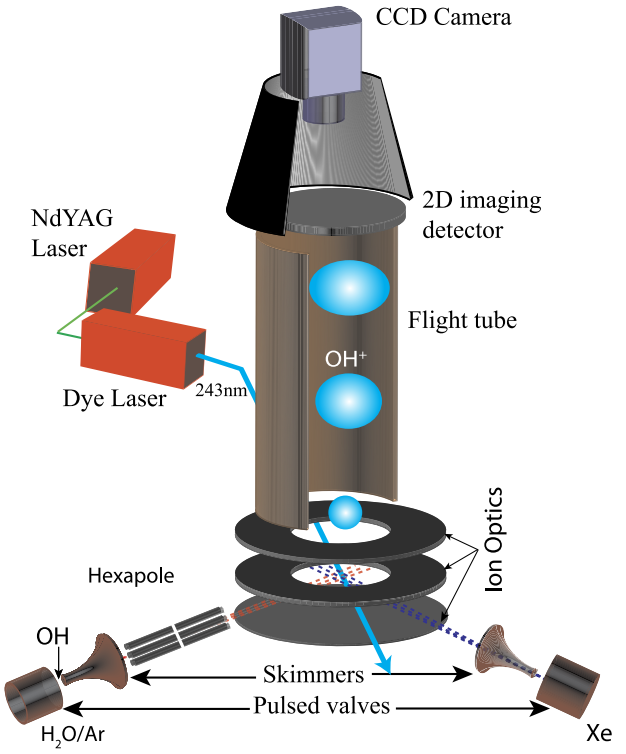

FIG. 1. Schematic of the crossed beam VMI setup showing two molecular beams crossing at the center of the imaging ion optics, consisting of three electrodes. The OH beam is collimated by a skimmer and crossed by a second skimmed beam of pure Xe. The OH molecule is ionized by radiation at a wavelength around 243 nm regions using a pulsed tunable dye laser beam that is frequency-doubled in a BBO (β-BaB_2O_4) crystal and focused at the center of ion optics by a 20 cm lens. The electric field vector of the linear polarized laser beam lies perpendicular to the collision plane. The nascent OH^+ image is mass-selected by time-of flight and projected onto a 2D imaging detector, then recorded by a CCD camera.

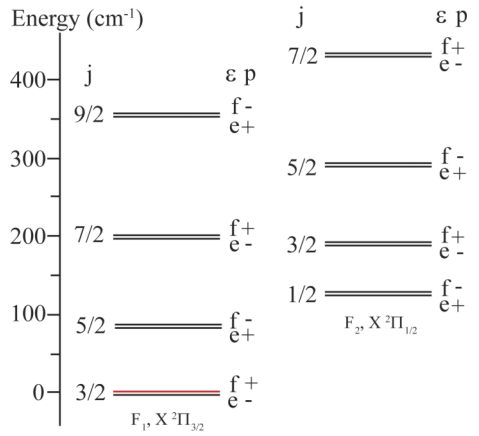

FIG. 2. Rotational energy levels for the electronic and vibrational ground state of OH. The energy states are labeled by total angular momentum j, Λ-doublet symmetry e ($\varepsilon = -1$) or f ($\varepsilon = 1$), and parity p. The energy difference between the Λ-doublet components is exaggerated for clarity. The red line shows the hexapole-selected OH($^2\Pi_{3/2}$, $\upsilon = 0$, j = 1.5f, +) level.

Downstream, the OH molecules enter a double hexapole state selector of 6 mm inner diameter. The two selectors are 12 cm long and consist of 6 cylindrical rods of 2.5 mm diameter. For better state selection, a beam stop of 2 mm diameter is placed on the molecular beam axis in front of the hexapole to block the molecules that fly along the central axis and do not experience any field from the state selector. The hexapole field focuses OH molecules in the low field seeking component, while it diverges the molecules in the high field seeking lower component of the Λ-doublet with parity = −1. After the hexapole, 97% of OH molecules are in the 1.5fF_1 level and 3% in the 1.5eF_1 level.

2. Differential cross section measurement setup

The OH molecules are scattered in a 90° crossed molecular beam arrangement. Because of the collision energy of 483 ± 40 cm^{-1}, the OH molecules can be excited to various rotational levels. Here, we study only the levels (in increasing energy) 1.5eF_1, 2.5eF_1, and 0.5eF_2. The rR_{11}(1.5), rR_{11}(2.5), and qR_{12}(0.5), $D^2\Sigma$-$X^2\Pi$ (0,0) [2 + 1] REMPI transitions were probed. The transitions are labeled as $\Delta N \Delta j$ F′ F″(j), where N is the total angular momentum excluding electron and nuclear spin, F is 1 or 2 for F_1 or F_2, and the single and double primes indicate upper and lower electronic states. The VMI technique was employed for measuring the velocity of the OH molecules after the collision. In this method, the ions produced by REMPI of neutral molecules are projected by an electric field to a two-dimensional (2D) position sensitive detector, usually micro-channel plates (MCPs). The heart of the technique lies

in the geometry of the electrostatic lenses that produce the electric field in such a way that any two particles of the same mass with the same velocity strike the detector at the same point, regardless of where they were formed. The evolving Newton spheres of these scattered molecules are projected to the detector. As the velocity of scattered molecules in the plane of collision is mapped onto the detector, we directly obtain the speed and angular information of the scattering process.

Our VMI setup (Fig. 1) contains ion optics, a time of flight (TOF) tube, and a two-dimensional detector that consists of MCP and phosphor screen. The ion optics consists of repeller, extractor, and ground electrode plates. These flat circular electrodes along with the two-dimensional detector lie parallel to the collision plane of our scattering studies, while the TOF axis lies perpendicular to the collision plane. The diameter of the ion optics plates is 80 mm, and the diameter of the opening in the extractor and ground plates is 20 mm, with separations between repeller-extractor and extractor-ground plates of 10 and 15 mm, respectively. The velocity mapping condition is obtained at a precise repeller-extractor voltage ratio, using 1000 and 776 V on the repeller and extractor plates, respectively. A charged coupled device (CCD) camera reads the signature of ions from Newton spheres of OH crushed on the 2D detector. All the ions with the same mass-to-charge ratio will fly along the time of flight tube (~350 mm) and arrive at the detector at the same time. At that moment, a positive pulse voltage of 850 V turns on the back plate of MCP for duration of 90 ns to select molecules of a given mass. The front plate of MCP and the phosphor screen are supplied with continuous potential of −850 V and +3500 V, respectively.

3. Integral cross section measurement setup

LIF was used to measure the total cross sections of OH(X) + Xe collision system. A detailed description of the experimental setup for LIF is given in previous reports,[11–13] and the initial OH populations in the OH beam were as reported by van Beek *et al.*[14] using double hexapole. The crossed molecular beam geometry was similar to the DCS measurement setup; however, the VMI ion optics were replaced by LIF detection system. A ring discharge was used instead of plate discharge arrangement of DCS measurements. At 15 mm from the valve nozzle, a stainless steel ring with an inner diameter of 3 mm was kept at −4 kV, producing an electrical discharge in the expanding mixture.

In order to reduce the presence of Xe clusters in the beam, the measurements were performed at only 800 millibars backing pressure, conditions at which less than 4% of the OH molecules were out-scattered from the $1.5fF_1$ level by collisions as observed in total cross section measurements. With this low parent beam density, the signal-to-noise ratio was consequently rather low.

B. Quantum scattering calculations

The methods used for the quantum scattering calculations were basically the same as those of previous papers.[8,10] Hence, only a brief description is provided here. The OH(X) – Xe PESs used here were those constructed by Groenenboom and co-workers.[5] The 4.4 version of the HIBRIDON program,[15] which uses the improved log-derivative propagator by Manolopoulos and co-workers,[16,17] was employed to propagate the wave function from $R = 3\alpha_0$ to $50\alpha_0$, where α_0 is the Bohr radius. The OH rotation, spin-orbit coupling, and Λ-doublet splitting parameters were those used in Ref. 8. The hyperfine structure of OH(X) was not taken into account.

ICSs and DCSs for collisions of $OH(1.5fF_1) + Xe$ at a collision energy of 490 cm^{-1} and 483 cm^{-1}, respectively, were calculated. Further calculations were performed around the mean experimental collision energies. Because of the negligible collision energy dependence on ICS/DCS, we did not average over the experimental collision energy spread. To converge the cross sections, a maximum value of total angular momentum ($J_{max} = 300.5$) and a maximum value of the rotational quantum number of the OH molecule ($j_{max} = 23.5$) were required. The calculated DCSs were obtained with resolution of 1°. In order to compare the system OH(X) – Xe with the OH(X) – He and examine the roles of the reduced mass in their different behaviour, three types of calculations were performed: (a) using OH(X) – Xe PES[5] and reduced mass $\mu = 15.0533$ amu as described above, (b) using OH(X) – He PES[18] and reduced mass $\mu = 3.2399$ amu, (c) using OH(X) – Xe PES[5] and a reduced mass of 3.2399 amu which corresponds to OH(X) – He.

III. RESULTS

A. Differential cross sections

In our crossed-beam velocity map imaging experiment, the DCS for scattering is obtained from the two-dimensional distribution of intensity from the projected image on the detector. To improve signal levels, the molecular beam angular spread is large, and there is also a rather wide longitudinal speed distribution of the molecules in the beam. The speed and angular spread cause a spread in the initial and final relative velocity vectors, thus lowering the angular resolution in the DCSs.

Newton diagrams representing the spread in the initial speeds of the two molecular beams (Xe and OH) based on a speed ratio, $v/\Delta v = 10$ (where v and Δv are the average speed and the width of the speed distribution in longitudinal direction, respectively) are shown in Fig. 3(a). The velocity vectors of the reactants and for the OH product scattered at 50° in the center-of-mass (CM) frame are drawn along with their distributions. Similar Newton diagrams representing the effect of the angular spread of the initial molecular beams are shown in Fig. 3(b). From geometrical consideration of the nozzle-skimmer distance and skimmer size, the angular spread in the Xe beam is 5.6°. For the OH beam, the 6 mm hole in the hexapole acts as a second collimator after the skimmer, resulting in a slightly better, 4°, angular spread. The 4° angular spread of the OH beam will be exactly mapped by the hexapole at the crossing position of the Xe and OH beams.

The dependence of the center-of-mass scattering angle spread on the molecular beam speed spreads and its angular

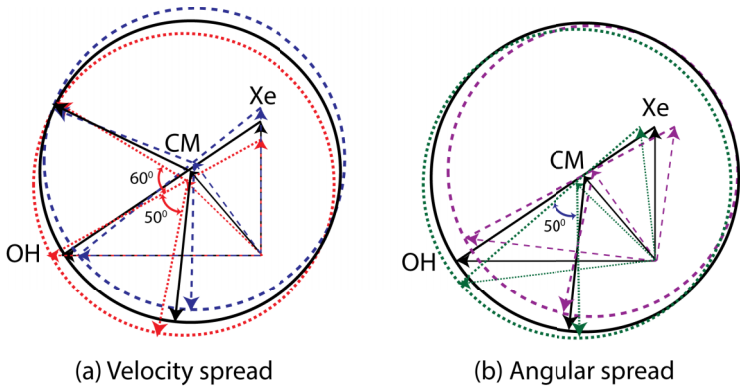

FIG. 3. Newton diagrams for OH + Xe collisions showing the two main kinematic sources of blurring in the angular resolution of DCSs: (a) the speed distribution caused by the longitudinal speed spread of OH and Xe beams for scattering angles of +60° (towards higher lab velocity) and −50° (towards lower lab velocity); (b) angular spreads in the collision plane, assuming the average velocities without a velocity spread.

divergence is shown in these Newton diagrams. At a given scattering angle, smaller or larger radii from the center-of-mass show the spread in energy. The blurring in the scattered product angular distribution due to velocity and angular spread depends strongly on the scattering angle. As shown in Fig. 3(a), the overlap of OH post-collision velocities shows much less angular blurring for scattering angles around +60° than at around −50° on the low lab velocity side.

We use REMPI to detect scattered product angular distributions in collision experiments where the molecules in the focal volume of the detection laser are probed. There is a kinematic problem involved in this kind of detection of the product angular distribution. Molecules that are moving along with the center-of-mass are faster than the molecules moving opposite to it and leave the detection volume. The molecules that are moving opposite to CM will be slower in the laboratory frame and will be detected with higher probability. This kind of preferential detection, which depends on the products' velocity in the lab frame, creates asymmetry in the images with respect to the relative velocity axis. This unwanted density build-up in the velocity map images should be corrected in order to obtain the actual product angular distribution. We apply the density to flux transformation using the IMSIM program[19] to extract DCSs correctly from velocity map images.

The IMSIM simulation uses the molecular speed distributions and the angular divergence of both the primary and secondary beams to simulate an image, thus allowing an estimation of the real angular resolution in the DCSs. In these simulations, linear combinations of all possible collision angles made by the molecular beam velocity vectors (as shown in Fig. 3(b)) that span angular spread of 6° for Xe and 4° for OH beam with a 1° step in the collision plane were employed. The angular resolution of the extracted experimental DCS of OH(X) + Xe was found to be 4°, 5°, 6°, and 10° for scattering angles between 0-75°, 75-105°, 105-135°, and 135-180°.

A comparison between experimental and theoretical OH($^2\Pi_{3/2}$, $\upsilon = 0$, $j = 1.5$) + Xe differential cross sections at a collision energy of 483 cm^{-1} is shown in Fig. 4 along with the experimental velocity mapped raw images. The DCSs from theory took into account that 97% of the OH molecules were initially in the $1.5fF_1$ level and 3% in the $1.5eF_1$ level. Theoretical results convoluted with the experimental resolution are also shown.

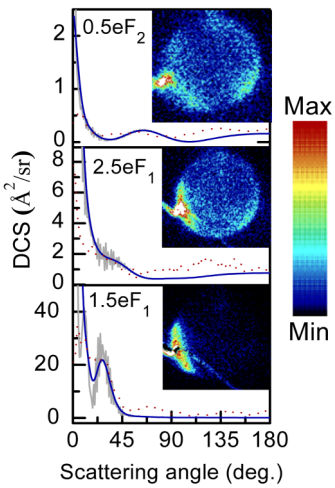

FIG. 4. Comparison between OH ($^2\Pi_{3/2}$, $\upsilon = 0$, $j = 1.5$) + Xe DCSs obtained at a collision energy of 483 cm^{-1} from experiments (red dotted line), theory with 1° resolution (light gray solid line), and theory convoluted with the experimental resolution (blue solid line). Using hexapole state selection, 97% of the initial OH population was in the $1.5fF_1$ level and 3% in the $1.5eF_1$. Experimental raw images and the OH rotational levels after the collision are also shown. The experimental DCSs have been multiplied by 5, 6, and 27 for the $1.5eF_1$, $2.5eF_1$, and $0.5eF_2$ levels, respectively.

B. Integral cross sections

A comparison between the experimental and theoretical state-to-state integral cross sections for the OH $(1.5fF_1) + Xe$ collisions at 490 cm^{-1} is shown in Fig. 5. The experiment provided only relative and not absolute values for the integral cross sections and thus have been rescaled to have the same sum as the theoretical ones. The decrease of the measured cross sections with the rotational excitation and the propensity for the spin-orbit conserving transitions are in very good agreement with the calculations. For the spin-orbit changing transitions, the experimental error bars are larger, but the general trends follow the theoretical ones. The measured values of the cross section for the transitions to the $1.5eF_2$ and $2.5eF_2$ levels include contributions from excitations to both rotational states, probed by transitions unresolved. In order to split this total unresolved signal into two separate components, the theoretical value of the ratio between these two cross sections was used.

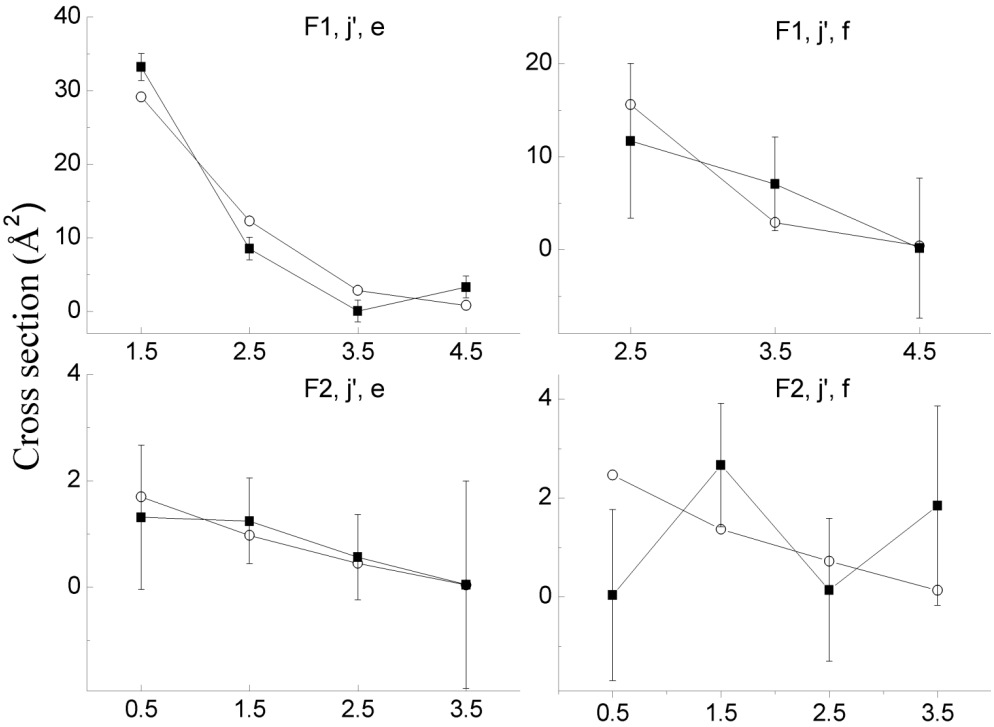

FIG. 5. State-to-state cross sections for OH ($^2\Pi_{3/2}$, υ = 0, j = 3/2, f) scattered by Xe at a collision energy of 490 cm^{-1}. The final spin-orbit manifold and Λ-doublet symmetry are indicated in the legend of the graphs, the final j′ quantum number is indicated on the abscissa. Values from the experiments (filled squares)[13] have been scaled to the theoretical values (open circles). The calculations have taken into account the initial (experimental) state populations.

IV. DISCUSSION

With this work on OH(X) + Xe together with previous work on OH(X) + Ar/He, we are able to examine common and different characteristics of OH(X) + Rg systems, where Rg is a rare gas atom. The collision of a hydroxyl molecule with a noble atom can be described by two adiabatic potential energy surfaces, of symmetry ^{2}A′ and ^{2}A″. In the former PES, the singly filled electron orbital lies in the O-H-Rg plane, and for the latter PES, it is perpendicular to it. In the scattering calculations, however, it is more convenient to use the two diabatic potentials: the sum potential $V_{sum} = 0.5(V_{A'} + V_{A''})$ and the difference potential $V_{diff} = 0.5(V_{A''} - V_{A'})$. These diabatic potentials are usually expanded as Legendre expansions,

$$V_{sum}(R,\theta) = \sum_{l=0}^{\infty} V_{l0}(R) d^l_{00}(\theta)$$

and

$$V_{diff}(R,\theta) = \sum_{l=2}^{\infty} V_{l2}(R) d^l_{20}(\theta),$$

where $d^l_{\lambda 0}(\theta)$ are the rotation matrix elements in the Jacobi angle θ and $V_{l\lambda}(R)$ are the radial expansion coefficients.[10,18,20,21] Plots of these coefficients for the He/Ar/Xe − OH(X) systems have been presented by McKendrick and co-workers.[10,20,21] The attractive well depth is around 60% deeper in Xe than in Ar, which is much more attractive than in He.[10] For Hund's case (a) molecules, the spin-orbit conserving transitions are dictated by the sum potential, and the spin-orbit transitions are mostly related to the difference potential. This description is less accurate for OH(X) molecule where for the low rotational levels is an intermediate case between Hund's cases (a) and (b).

As shown in Fig. 5, there is a general decrease of the integral cross sections with the final rotational quantum number. The ICS values for spin-orbit conserving transitions are much smaller than the values of the spin-orbit changing transitions. Theory represents these trends well; however, the agreement with experiment is not as good as in the OH(X) + He/Ar systems. These differences between experimental and theoretical OH(X) + Xe integral cross sections had also been observed for transitions to eF_2 levels by Gilijamse *et al.*[5] and in a more recent work by Scharfenberg *et al.*[7] where the experimental uncertainties were much larger for spin-orbit changing collisions. The present results on integral cross sections[13] are in less good agreement with theory than in previous work[5,7] performed at lower collision energies. The reason for this deviation is not yet clear. Although the formation of Xe dimers is hard to avoid, it should not be an explanation because the backing pressure for our experiments is about three times lower than in previous work.[5,7] Since our experiments are at higher collision energies than previous work, a possible explanation could be that the PES can be improved at short intermolecular distances and especially for the potential terms that lead to spin-orbit changing transitions. As it was anticipated, the ICS values for OH(X) + Xe are significantly larger than those for OH(X) + Ar, which are much larger than OH(X) + He. For example, the calculated value of ICS for the Λ-doublet changing OH(1.5eF_1) + Xe collision is around 28 Å,^{2} which is around twice of the corresponding collision with Ar and around 28 times larger than those with He. We refer the interested reader to Ref. 10

for the explanation of this difference in terms of the relative radial expansion coefficients in the corresponding PES.

As shown in Fig. 4, the measured differential cross sections reveal that the collisions are forward scattered. The theoretical calculations reproduce very well the experimental values except at the smallest forward angles where the experimental background subtraction procedure is least reliable.[8] The OH(X) + Xe DCS measured at 490 cm^{-1} from this work is quite similar to OH(X) + Ar DCS obtained by Sarma *et al.* at the rather similar collision energy of 500 cm^{-1}.[8] The only significant difference here is that the OH(1.5eF$_1$) + Xe Λ-doublet changing transition from this work is more backward scattered than those with Ar, which was found more backward than those with He.[8] We also note that the agreement between theoretical and experimental DCS is somewhat worse for collisions with Xe than was previously observed with Ar or He. The full set of theoretical DCS for all open channels from the OH(1.5eF$_1$) level is provided in the supplementary material.[22]

Dagdigian and Alexander[23–25] by decomposing the integral cross sections into total angular momentum dependent contributions used these partial cross sections (PCSs) to shed light on the stereodynamics of OH(X) + Ar/He Λ-doublet changing collisions. They found that the PCS for He has two peaks, one around 3 Å and one around 6-7 Å (which is in the attractive part of the potential) at collision energy of 300 cm^{-1}. For Ar, however, there is only narrow peak at around 8 Å. Following their methodology, we present the full set of theoretical PCS for all possible final products for scattering of OH(1.5eF$_1$) with Xe at collision energy of 490 cm^{-1} in the supplementary material.[22] These partial cross sections can be compared with the full set of partial cross sections for OH(X) + Ar/He scattering at collision energies of 500 and 460 cm^{-1}, respectively, which are shown in the supplementary material in the paper by Sarma *et al.*[8] Like those PCS for collisions with Ar, the PCS for collisions with Xe has much richer structure than the PCS for He and shows multiple peaks for many final rotational levels. For collisions leading to the same spectroscopic parity, for example, eF$_2$, the peak(s) of the PCS move to lower J_{tot} values, where J_{tot} is the total angular momentum. This is consistent with the semiclassical picture that the more inelastic collisions take place through trajectories that exhibit opacity functions with peaks at low impact parameters, thus sampling the repulsive part of the potential.

In order to disentangle the role of the mass from the role of the PES, additional calculations were performed where the OH(X) – Xe PES was used in combination with the reduced mass of OH – He (instead of OH – Xe); we will refer to this artificial atom as "Xe," hereafter. The reduced mass of OH – Xe is around 4.6 times larger than of OH-"Xe." Thus, for the same collision energy, the mean relative speed of Xe – OH would be $(\mu_{HeOH}/\mu_{XeOH})^{1/2}$ smaller than that of "Xe" – OH. The ratio of the sum of the Xe + OH(X) ICS versus the corresponding sum of the "Xe" + OH(X) ICS is around 1.34. The ratio of the sum of the "Xe" + OH(X) ICS versus the corresponding sum of the He + OH(X) is around 3.66. The full set of theoretical DCS and PCS is available in the supplementary material,[22] and we present here the DCS only for the final rotational levels that were measured experimentally in this work. As shown in Fig. 6, collisions with "Xe" are more backwards than collisions with Xe for the OH(0.5eF$_2$) final level, but the differences become much less pronounced for the OH(1.5eF$_1$) and OH(2.5eF$_1$) final levels. The differences between Xe + OH(X) and "Xe" + OH(X) collisions are more clear in plots of PCS,[22] where "Xe" + OH(X) PCS is always between those of Xe + OH(X) and He + OH(X). In most of the cases, the peaks of "Xe" + OH(X) PCS correspond to J_{tot} values that are half of those of Xe + OH(X).

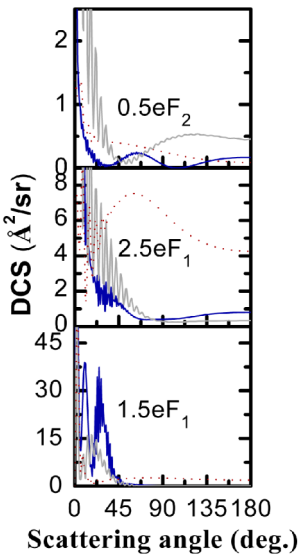

FIG. 6. Comparison between OH($^2\Pi_{3/2}$, υ = 0, j = 1.5f) + X DCSs calculated at a collision energy of 490 cm^{-1} from collisions: (a) with He (red dotted line) using the OH(X) – He PES from Ref. 18, (b) with Xe (blue solid line) using the OH(X) – Xe PES from Ref. 5, and (c) with Xe (light grey solid line) using the OH(X) – Xe PES from Ref. 5 and a reduced mass that corresponds to OH(X) – He. The DCSs for collisions with He (red dotted line) have been multiplied by 15 for the 2.5eF$_1$ and by 30 for 1.5eF$_1$ levels.

V. CONCLUSIONS

Differential cross sections for fully quantum state selected OH molecules ($^2\Pi_{3/2}$, υ = 0, j = 1.5f) colliding with Xe atoms were obtained using the hexapole electric field selection method combined with resonance-enhanced multiphoton ionization and velocity-map imaging. These experimental results together with recent measurements of integral cross sections were compared with theoretical calculations. This was very useful to test the only available *ab initio* potential energy surface. The experimental results correspond well to those calculated using exact close coupling calculations. The agreement between experimental and theoretical integral cross sections is less satisfactory at high collision energies than at low collision energies[5,7] and for spin-orbit changing collisions than for spin-orbit conserving transitions. The agreement between experimental and theoretical differential cross sections is better for sideways scattering than for extreme forward collisions. All these not only lend support to the validity of the *ab initio* potential energy surface but also indicate that perhaps further improvement is possible, especially at short intermolecular seperations and for the

V_{diff} potential of a system where relativistic effects may be important. Although this limited set of measurements cannot act as a thorough test of the Xe – OH PES, we note that the agreement between experiment and theory is better for the integral cross sections in the He/Ar + OH systems than in Xe + OH. Possible reasons for this discrepancy might lie in the experimental side either because of the low signal-to-noise ratios in the Xe + OH measurements or because of the unwanted, limited presence of Xe clusters. Future calculations on collisions of OH(X) with Xe clusters, such as Xe_2, will help to examine the effects of clusters on the DCS. We can point out, however, that recoil from a Xe_n, with $n > 1$, cluster would lead to a much larger OH image than is observed. This work on Xe + OH, together with our previous work on He/Ar + OH, demonstrates that it is feasible to bring hydroxyl radical within the scope of the VMI technique. The extension of this work to collisions of OH radicals with diatomic and polyatomic molecules will provide valuable information in a wide range of chemical processes where the OH is a key species.

ACKNOWLEDGMENTS

The authors thank Dr Angelica Moise for her many contributions to this work. Research in Nijmegen was supported by the Netherlands NWO-CW Project No. 700.58.029, the Dutch Astrochemistry Network, and the EU-ITN Network "ICONIC" 238671. S.M. was supported by the British Council-Platform Bèta Techniek Programme in Science while he was funded by an EPSRC Grant No. EP/H008403/1 awarded to Professor Brian J. Howard (Oxford University). We acknowledge M. H. Alexander (Maryland) and P. J. Dagdigian (Johns Hopkins) for providing the latest version of Hibridon and J. Kłos (Maryland) and S. Stolte (Jilin) for useful discussions. This research utilized Queen Mary's MidPlus computational facilities, supported by QMUL Research-IT and funded by EPSRC Grant No. EP/K000128/1.

[1]B. J. Robinson and R. X. McGee, Annu. Rev. Astron. Astrophys. **5**, 183 (1967).
[2]A. Brockhinke, U. Lenhard, A. Bülter, and K. Kohse-Höinghaus, Phys. Chem. Chem. Phys. **7**, 874 (2005).
[3]D. E. Heard, Annu. Rev. Phys. Chem. **57**, 191 (2006).
[4]J. M. Brown and A. Carrington, *Rotational Spectroscopy of Diatomic Molecules* (Cambridge University Press, Cambridge, 2003).
[5]J. J. Gilijamse, S. Hoekstra, S. Y. T. van de Meerakker, G. C. Groenenboom, and G. Meijer, Science **313**, 1617 (2006).
[6]L. Scharfenberg, J. Kłos, P. J. Dagdigian, M. H. Alexander, G. Meijer, and S. Y. T. van de Meerakker, Phys. Chem. Chem. Phys. **12**, 10660 (2010).
[7]L. Scharfenberg, K. B. Gubbels, M. Kirste, G. C. Groenenboom, A. van der Avoird, G. Meijer, and S. Y. T. van de Meerakker, Eur. Phys. J. D **65**, 189 (2011).
[8]G. Sarma, S. Marinakis, J. J. ter Meulen, D. H. Parker, and K. G. Mckendrick, Nat. Chem. **4**, 985 (2012).
[9]M. L. Costen, S. Marinakis, and K. G. McKendrick, Chem. Soc. Rev. **37**, 732 (2008).
[10]G. Paterson, S. Marinakis, J. Klos, M. L. Costen, and K. G. McKendrick, Phys. Chem. Chem. Phys. **11**, 8804 (2009).
[11]M. C. van Beek, J. J. ter Meulen, and M. H. Alexander, J. Chem. Phys. **113**, 637 (2000).
[12]A. Moise, R. Cireasa, D. H. Parker, and J. J. ter Meulen, J. Chem. Phys. **125**, 204315 (2006).
[13]A. V. Moise, *Scattering of State-Selected and Oriented Hydroxyl Radicals by Halogen Hydrides and Xenon* (Radboud University Nijmegen, Nijmegen, 2007), available at http://hdl.handle.net/2066/30159.
[14]M. C. van Beek, J. J. ter Meulen, and M. H. Alexander, J. Chem. Phys. **113**, 628 (2000).
[15]HIBRIDON is a package of programs for the time-independent quantum treatment of inelastic collisions photodissociation written by M. H. Alexander D. Manolopoulos H.-J. Werner B. Follmeg with contributions by P. F. Vohralik, D. Lemoine, G. Corey, R. Gordon, B. Johnson, T. Orlikowski, A. Berning, A. Degli-Esposti, C. Rist, P. Dagdigian, B. Pouilly, G. van der Sanden, M. Yang, F. de Weerd, S. Gregurick, and J. Kłos 2015.
[16]D. E. Manolopoulos, J. Chem. Phys. **85**, 6425 (1986).
[17]M. H. Alexander and D. E. Manolopoulos, J. Chem. Phys. **86**, 2044 (1987).
[18]H.-S. Lee, A. B. McCoy, R. R. Toczyłowski, and S. M. Cybulski, J. Chem. Phys. **113**, 5736 (2000).
[19]G. C. McBane, *IMSIM program, version 2.0,* see http://faculty.gvsu.edu/mcbaneg/.
[20]G. Paterson, S. Marinakis, M. L. Costen, K. G. McKendrick, J. Kłos, and R. Toboła, J. Chem. Phys. **129**, 074304 (2008).
[21]G. Paterson, S. Marinakis, M. L. Costen, K. G. Mckendrick, J. Kłos, and R. Toboła, J. Chem. Phys. **131**, 159901 (2009).
[22]See supplementary material at http://dx.doi.org/10.1063/1.4906070 for a complete list of figures for DCSs and PCSs.
[23]P. J. Dagdigian and M. H. Alexander, J. Chem. Phys. **130**, 094303 (2009).
[24]P. J. Dagdigian and M. H. Alexander, J. Chem. Phys. **130**, 164315 (2009).
[25]P. J. Dagdigian and M. H. Alexander, J. Chem. Phys. **131**, 229902 (2009).